



Article

Investigation of the Effect of Molybdenum Silicide Addition on the Oxidation Behavior of Hafnium Carbonitride

Veronika Suvorova ^{1,*}, Andrey Nepapushev ¹, Dmitrii Suvorov ², Kirill Kuskov ^{1,2}, Pavel Loginov ³
and Dmitry Moskovskikh ¹

¹ Center of Functional Nano-Ceramics, National University of Science and Technology MISiS, Leninskiy Prospekt, 4, 119049 Moscow, Russia

² Department of Functional Nanosystems and High Temperature Materials, National University of Science and Technology MISiS, Leninskiy Prospekt, 4, 119049 Moscow, Russia

³ Scientific-Educational Center of SHS, National University of Science and Technology MISiS, Leninskiy Prospekt, 4, 119049 Moscow, Russia

* Correspondence: buynevich.vs@misis.ru

Abstract: In this study, the oxidation stability up to 1000 °C in air of the Hf(C,N)-MoSi₂ composites was explored under non-isothermal and isothermal conditions. Composites with 1, 5, 10, and 20% volume fractions were produced by low-energy ball milling and subsequent spark plasma sintering. Differential scanning calorimetry (DSC) and thermogravimetric (TG) coupled with mass spectrometry were used to reveal the staging of the oxidation process depending on the additive content. It was found that samples containing 1 and 5 vol% MoSi₂ had the lowest weight gain and the best oxidation behavior. The results of this study were supported by microstructural and phase analyses of the samples after isothermal treatment in a furnace. The samples with the lowest molybdenum disilicide content had a dense and thin protective oxide film on the surface, consisting of hafnium orthosilicate and monoclinic HfO₂. The increase in the amount of MoSi₂ contributed to the formation of a loose and porous oxide layer due to the increase in the concentration of volatile MoO₃. However, all samples exhibited higher oxidation resistance compared to the pure Hf(C,N).

Keywords: ultra-high-temperature ceramics; hafnium carbonitride; composites; spark plasma sintering; oxidation behavior



Citation: Suvorova, V.; Nepapushev, A.; Suvorov, D.; Kuskov, K.; Loginov, P.; Moskovskikh, D. Investigation of the Effect of Molybdenum Silicide Addition on the Oxidation Behavior of Hafnium Carbonitride. *J. Compos. Sci.* **2023**, *7*, 25. <https://doi.org/10.3390/jcs7010025>

Academic Editor: Dshetti Jampaiah

Received: 20 November 2022

Revised: 20 December 2022

Accepted: 6 January 2023

Published: 10 January 2023



Copyright: © 2023 by the authors. Licensee MDPI, Basel, Switzerland. This article is an open access article distributed under the terms and conditions of the Creative Commons Attribution (CC BY) license (<https://creativecommons.org/licenses/by/4.0/>).

1. Introduction

For effective protection against high-intensity thermal loads ($T > 2000$ °C), materials with high erosion and oxidation resistance, high mechanical properties, as well as high thermal conductivity, are required to remove heat from the most heat-loaded units to the “cold” load-bearing assemblies of an aircraft. The most suitable compounds for high-temperature applications are ultra-high temperature ceramics (UHTC) [1–3], in particular, transition metal carbonitrides [4–7] due to their high thermal stability. Numerous publications [8–11] suggest that the introduction of nitrogen atoms into the carbide sublattice promotes an increase in the melting temperature, mechanical, and thermophysical properties, as well as oxidative resistance, due to the hybridization of electron orbitals upon substitution of atoms in the metallic and nonmetallic sublattices and due to the phenomenon of solid solution hardening. It was previously demonstrated in an earlier study that the introduction of nitrogen into the HfC lattice contributes to an increase in the melting point [12]. Furthermore, hafnium carbonitride HfC_{0.5}N_{0.35}, obtained by a combination of mechanical activation, combustion synthesis, and spark plasma sintering, exhibited high hardness and crack resistance. However, like most UHTCs, Hf(C,N) is actively oxidized in air with the formation of a highly porous cracking layer consisting of monoclinic HfO₂ ($k_p = 10^{-7}$ g²·cm⁴·s⁻¹ [13]).

Si-containing additives, such as SiC and MoSi₂, are usually added to UHTC, which contributes to the formation of a protective MeSiO₄ orthosilicate with a low oxygen diffusion rate ($k_p = 10^{-11}$ g²·cm⁴·s⁻¹) [13]. The introduction of silicon carbide into Hf(C,N) has

already been proven to be an effective method of protecting against oxidation due to the formation of a complex oxide layer. This layer is composed of silicates consisting of HfSiO_4 and $\text{Si}_{1-x}\text{Hf}_x\text{O}_2$, which fill the HfO_2 skeleton and promote the healing of microcracks and pores [14].

Molybdenum disilicide is also a worthy candidate for use as an additive for protection against oxidation [15–20]. It is characterized by high oxidation and thermal stabilities and has the highest melting point (2030 °C) among silicides [18,21]. Chen et al. [15] developed HfC-MoSi₂ protective coatings for C/C-SiC composites with different MoSi₂ contents. The introduction of molybdenum disilicide significantly increased the ablation resistance due to the formation of a dense multiphase Hf-Si-O layer, in which the pores and cracks are healed by the liquid phases of SiO₂ and HfSiO₄, preventing oxygen diffusion. A HfC-MoSi₂ coating with 25 vol% MoSi₂ provided more effective protection of C/C-SiC against ablation compared to a HfC-SiC. It is expected that the introduction of MoSi₂ to the ultra-high-temperature ceramic Hf(C,N) will improve its oxidation resistance.

Bulk Hf(C,N)-MoSi₂ composites were prepared by mixing MoSi₂ and Hf(C,N) powders in a high-energy planetary ball mill followed by spark plasma sintering. In this work, the influence of MoSi₂ on the oxidation resistance of Hf(C,N) was investigated under non-isothermal and static conditions.

2. Materials and Methods

2.1. Powder Preparation

The introduction of different MoSi₂ (TU 6-09-03-395-74, 99% “Plasmotherm”) content (1, 5, 10, and 20 vol%, referred to as HfCN1M, HfCN5M, HfCN10M, and HfCN20M further in the manuscript, respectively) to the synthesized hafnium carbonitride Hf(C,N) was carried out in a high-energy planetary ball mill Activator-2S (LLC Activator, Novosibirsk, Russia) in an argon atmosphere (purity 99.998%). All experiments were conducted with a ball-to-powder mass ratio of 20:1 (360 g: 18 g) in 250 mL steel jars. The jars were first evacuated using a vacuum pump, and then argon gas was pumped into the jars until the pressure reached 0.6 MPa. The mixing was carried out for 10 min at a planetary disc and jar rotation speed of 347 rpm.

2.2. Sintering

Powder mixture consolidation was performed using a Spark Plasma Sintering Unit Labox 650 (SinterLand, Nagaoka, Japan). A 3 g powder mixture was placed into a graphite die with graphite paper inside it. To improve heat retention during the sintering process, a heat-insulating fabric (graphite felt) was used. The die, which contained powder, was fed into the hydraulic system between two electrodes. The powder mixture was then subjected to a pressure of 10 MPa. The SPS chamber was evacuated and then filled with argon. All sintering was conducted under a load of 50 MPa and a holding time of 20 min. The heating rate was 100 °C/min. The sintering temperature was 2000 °C. The samples were cooled during the installation. As a result of sintering, samples with a diameter of 12 mm and a thickness of 5 to 10 mm were obtained.

2.3. Characterization

The phase composition of the samples after SPS was studied by X-ray phase analysis (XRD). X-ray spectra were obtained on a Diffractometer DIFREY-401 (JSC Scientific Instruments, Saint Petersburg, Russia) with Cr-K α radiation ($\lambda = 0.22909$ nm) in the step-by-step scanning mode (shooting step was 0.1°) in the angle range from 30 to 110° with a 2 s exposure. The phase composition of the synthesized and compacted samples was identified using the PDF 2 (2004) databases. The microstructure of the consolidated ceramics and their elemental composition were studied using a JEOL JSM7600F scanning electron microscope (JEOL Ltd., Tokyo, Japan) with an INCA SDD 61 X-MAX energy dispersive attachment (Oxford Instruments, UK) in the backscattered electron mode at an accelerating voltage of 15 kV (resolution 3 nm). The density (ρ_h) of the compact ceramic materials was determined

by hydrostatic weighing according to at least ten measurements in air and in distilled water ($\rho_w = 0.9978 \text{ g/cm}^3$). Vaseline ($\rho_p = 0.870 \text{ g/cm}^3$) acted as a layer covering the open porosity. The density was calculated according to the formula:

$$\rho_h = \frac{m_1 \rho_w \rho_p}{(m_2 - m_3) \rho_p - m_4 \rho_p} \quad (1)$$

where ρ_h is the sample's density, g/cm^3 ; ρ_w is the density of water, g/cm^3 ; ρ_p is the layer density, g/cm^3 ; m_1 is the mass of the sample in air, g; m_2 is the mass of the sample with vaseline in air, g; m_3 is the mass of the sample with vaseline in water, g; m_4 is the mass of vaseline ($m_2 - m_1$), g.

Weighing was carried out on a Precisa ES 220A analytical balance (Precisa, Switzerland) with a measurement error of $\pm 0.0001 \text{ g}$.

The true density (ρ_t) of sintered ceramic materials was measured on an AccuPyc1340 helium pycnometer (Micromeritics, Austria).

The relative density (ρ) was calculated using the following formula:

$$\rho = \frac{\rho_h}{\rho_t} \times 100\% \quad (2)$$

where ρ is the relative density, %; ρ_h is the value of hydrostatic density, g/cm^3 ; ρ_t is the value of true density, g/cm^3 ;

The hardness of the consolidated materials was measured using a digital hardness tester, Durascan—70 (Struers ApS, Ballerup, Denmark), using the Vickers method. The hardness (HV) was calculated using the following formula:

$$\text{HV} = 1.854 \cdot \frac{P}{d^2}, \quad (3)$$

where H is the Vickers hardness, GPa; P is the load applied to the indenter, N; and d is the diagonal of the rhombus, m.

2.4. Thermogravimetric Analysis

The thermogravimetric analysis of the sintered ceramics was carried out on a NETZSCH STA 409 PC Luxx synchronous analyzer (NETZSCH-Gerätebau GmbH, Selb, Germany) equipped with a NETZSCH QMS 403 Aëolos quadrupole mass spectrometer. The experiments were carried out in an air atmosphere with an air flow of 50 mL/min. Samples weighing $30 \pm 5 \text{ mg}$ in Al_2O_3 crucibles were heated to $1000 \text{ }^\circ\text{C}$ at a rate of $20 \text{ }^\circ\text{C/min}$.

2.5. Static Oxidation

To study structural changes during the oxidation process, rectangular parallelepiped-shaped samples of Hf(C,N) and Hf(C,N)- MoSi_2 were kept in an SShOL 1.1.6/12-M3 electric furnace (Tula-Term, Russia) at $1000 \text{ }^\circ\text{C}$ for 30 min. The samples were initially polished on a Tegramin grinding and polishing machine (Struers, Copenhagen, Denmark). To carry out the experiment under the same conditions for all samples, the samples were placed on the same platform in a furnace in alundum crucibles.

3. Results

3.1. Spark Plasma Sintering

Figure 1 shows the typical microstructures of bulk Hf(C,N)- MoSi_2 samples with different MoSi_2 content obtained by spark plasma sintering. Similar microstructures characterize all samples. As evident from the SEM images (Figure 1a,d,g,j), the contrast in the HfCN1M, HfCN5M, HfCN10M, and HfCN20M samples is due to the presence of several phase components, including Hf(C,N) (red areas), monoclinic and tetragonal HfO_2 (green and yellow areas), MoSi_2 (blue areas), and (Fe,Cr) (black areas). Regardless of the amount of additive, the grain size of the main Hf(C,N) phase varies from 2 to $15 \text{ }\mu\text{m}$ with an aver-

age grain size of 7 μm . The oxide inclusions are predominantly located along the grain boundaries of the main Hf(C,N) phase. The presence of iron inclusions is associated with the preliminary mechanical activation of the hafnium powder mixture with carbon in steel jars with steel grinding balls [12]. Furthermore, pores up to 2 μm in size are found in the samples, both inside the grains and along their boundaries. According to the EBSD images (Figure 1c,f,i,l), the Hf(C,N) and MoSi₂ grains have different crystallographic orientations that are randomly distributed.

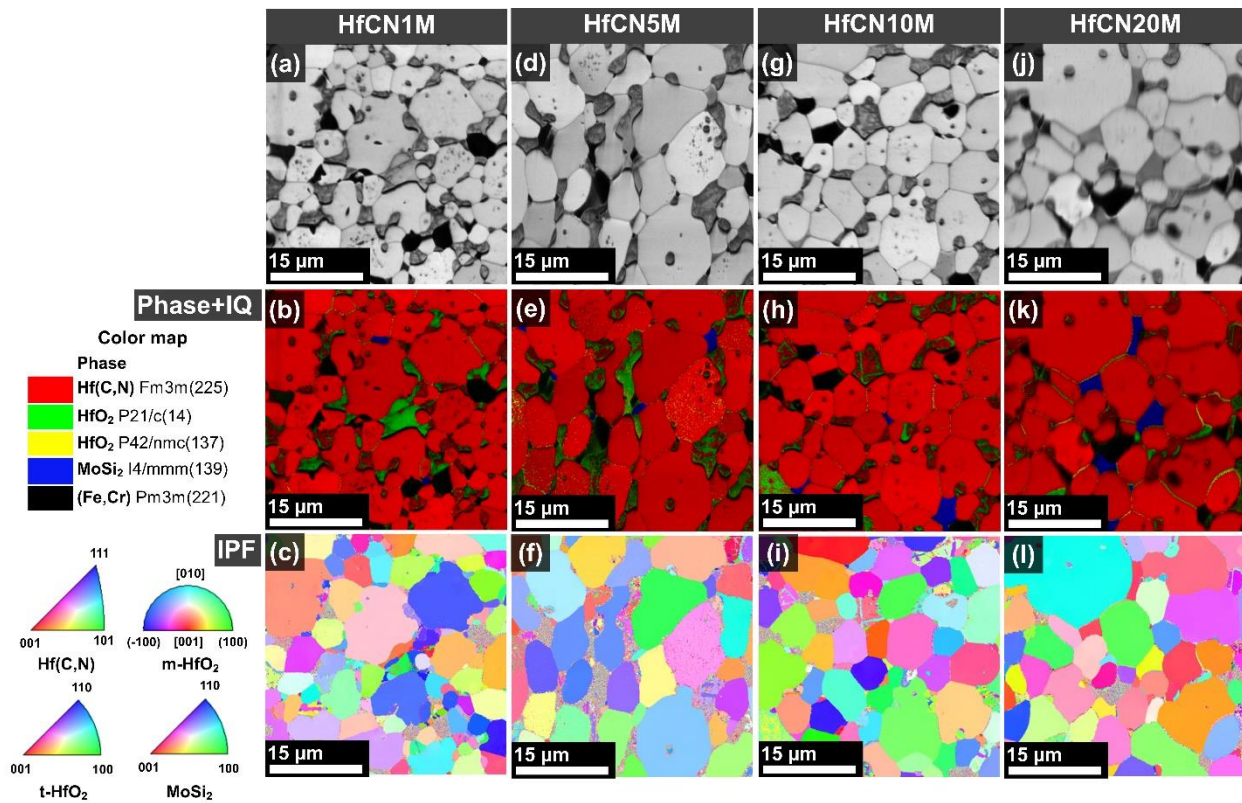


Figure 1. Micrographs and EBSD images of the Hf(C,N)-MoSi₂ samples with different MoSi₂ content: (a–c) 1 vol%; (d–f) 5 vol%; (g–i) 10 vol%; (j–l) 20 vol%.

Since the diffraction patterns of samples with different MoSi₂ contents are similar, Figure 2 shows the diffraction patterns of sintered MoSi₂, Hf(C,N) [12], and HfCN20M as typical ones. Intense peaks correspond to the Hf(C,N) phase of the NaCl Fm3m (225) structural type. All samples contain hafnium oxide peaks of two structural types: tetragonal P42/nmc (137) and monoclinic P21/c (42). It appears that there are no MoSi₂ reflections in the HfCN20M pattern, which is likely due to the low intensity of MoSi₂ reflections compared to other phases. The absence of MoSi₂ solubility in the Hf(C,N) lattice is confirmed by the invariance of the Hf(C,N) lattice parameter after the introduction of MoSi₂ (Table 1).

Table 1. D-spacing for the bulk Hf(C,N) and Hf(C,N)-MoSi₂.

Material	NaCl Fm3m(225)					a, nm
	(111)	(200)	(220)	(311)	(222)	
Hf(C,N)	2.6501	2.292	1.6232	1.386	1.3251	0.459
HfCN20M	2.6448	2.2905	1.6224	1.3851	1.3246	0.459

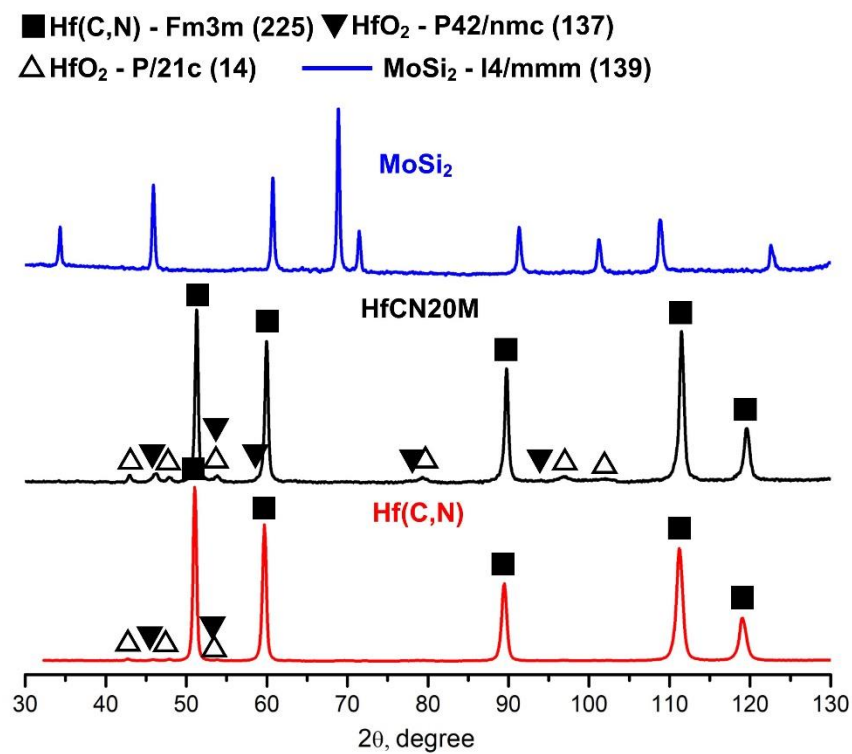


Figure 2. X-ray diffraction patterns of MoSi_2 , Hf(C,N) , and HfCN20M samples.

The density and mechanical property values for bulk ceramics are presented in Table 2. The measured density values (more than 98%) are in good agreement with the structure of bulk materials (Figure 1). The hardness of the Hf(C,N) - MoSi_2 ceramics is comparable to those of similar materials [22–24]. It is worth noting that the introduction of MoSi_2 leads to a slight decrease in hardness when compared to pure Hf(C,N) [12].

Table 2. Mechanical properties of composites with MoSi_2 .

Material	Density, ρ_h ($\text{g}\cdot\text{cm}^{-3}$)	Relative Density (%)	Hardness, HV (GPa)
Hf(C,N) [12]	-	98.1	21.3 ± 0.55
HfCN1M	11.76 ± 0.06	98.6 ± 0.8	19.2 ± 0.3
HfCN5M	11.83 ± 0.06	98.5 ± 0.9	18.1 ± 0.2
HfCN10M	11.28 ± 0.06	98.6 ± 0.6	17.7 ± 0.5
HfCN20M	11.42 ± 0.06	98.2 ± 0.6	16.9 ± 0.3
$\text{HfC} + 5\text{MoSi}_2$ [22]	11.80	93	17.84 ± 1.45
$\text{HfC} + 15 \text{ vol}\% \text{ MoSi}_2$ [23]	11.7	99.9	19.6 ± 0.5
$\text{HfC} + 10 \text{ vol}\% \text{ MoSi}_2$ [24]	11.79	97.8	16.1 ± 0.4
$\text{HfC} + 20 \text{ vol}\% \text{ MoSi}_2$ [24]	11.01	96.5	15.5 ± 0.9
$\text{HfC} + 1 \text{ vol}\% \text{ MoSi}_2$ [22]	12.3	98.0	21.1 ± 0.7

3.2. Oxidation Behavior

Figure 3 illustrates thermogravimetric curves that describe the change in sample mass depending on temperature during the non-isothermal oxidation of Hf(C,N) and Hf(C,N) - MoSi_2 sintered ceramics. The samples were heated to 1000 °C in air at 20 °C/min. The weight gain from oxidation begins at approximately 720 °C for all compositions, but the inflection temperature varies depending on the composition.

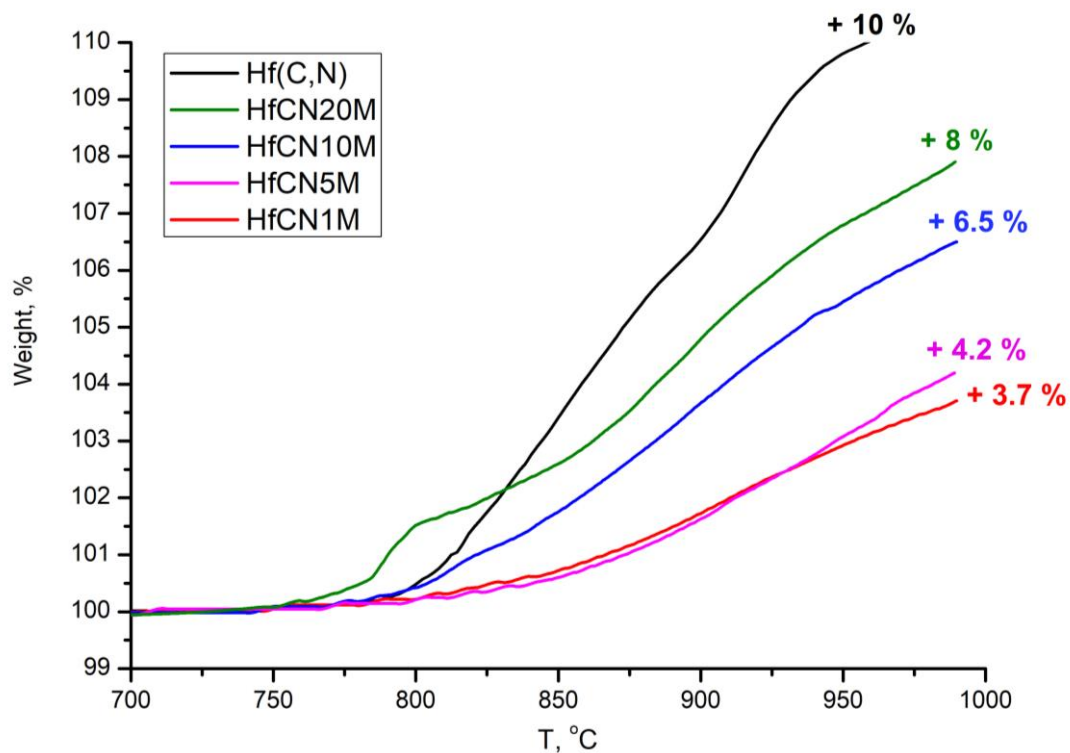


Figure 3. Thermogravimetric curves of Hf(C,N) and Hf(C,N)-MoSi₂ samples.

In the case of the Hf(C,N) sample, one can observe an inflection in the TG curve at 800 °C; up to this point, oxidation proceeds slowly. At temperatures above this point, the oxidation significantly accelerates, and at 960 °C, Hf(C,N) is completely oxidized with a weight gain of 10%. Low concentrations of MoSi₂ (1 and 5 vol%) contribute to an increase in the onset of oxidation to 840 °C and a decrease in the oxidation rate. Therefore, the HfCN1M and HfCN5M samples are characterized by the smallest gains, which are 3.7% and 4.2%, respectively. When the MoSi₂ concentration is increased to 10 and 20 vol%, the inflection temperature decreases to 810 °C and 785 °C, respectively. Between 810 and 990 °C, the oxidation rate of the HfCN10M sample is significantly lower than that of Hf(C,N); its weight gain was 6.5%. A sample with the highest MoSi₂ concentration during oxidation displays complex behavior. In the temperature range from 720 °C to 785 °C, the oxidation rate of HfCN20M is almost six times higher than the oxidation rate of the other samples. Active oxidation becomes slower at 800 °C but accelerates again at the point corresponding to 860 °C. Despite the periodic acceleration of oxidation, the weight gain at 990 °C was 8%, which is 2% lower than the weight gain of pure Hf(C,N).

Figure 4 illustrates the thermal changes that occurred during the oxidation of Hf(C,N) and Hf(C,N)-MoSi₂. In all samples, the onset of the exothermic reaction was observed at 725 °C, which is in good agreement with the temperature on the TG curves (Figure 3). In the case of Hf(C,N), HfCN1M, and HfCN5M samples, a gradual increase in the thermal effect of the exothermic reaction is observed with an increase in temperature. According to mass spectroscopy (MS, Figure 5), the onset of Hf(C,N) oxidation at 725 °C is accompanied by the formation of NO ($m/z = 30$) and, to a lesser extent, NO₂ ($m/z = 46$). This is evidenced by an increase in the values of ionic current on the mass spectra of NO and NO₂. With a slight delay, a gradual release of CO₂ ($m/z = 44$) is observed, which reaches its maximum at 910 °C. CO emissions were not detected.

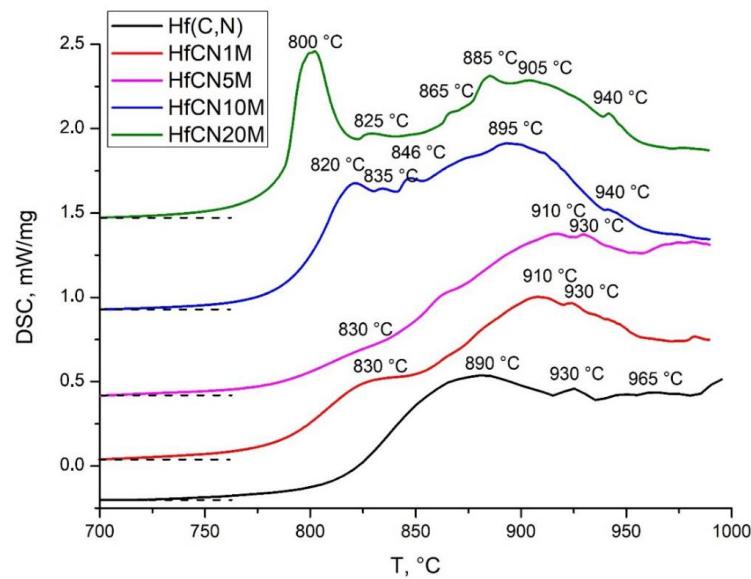


Figure 4. DSC curves during the oxidation of bulk Hf(C,N) and Hf(C,N)-MoSi₂ upon heating to 1000 °C.

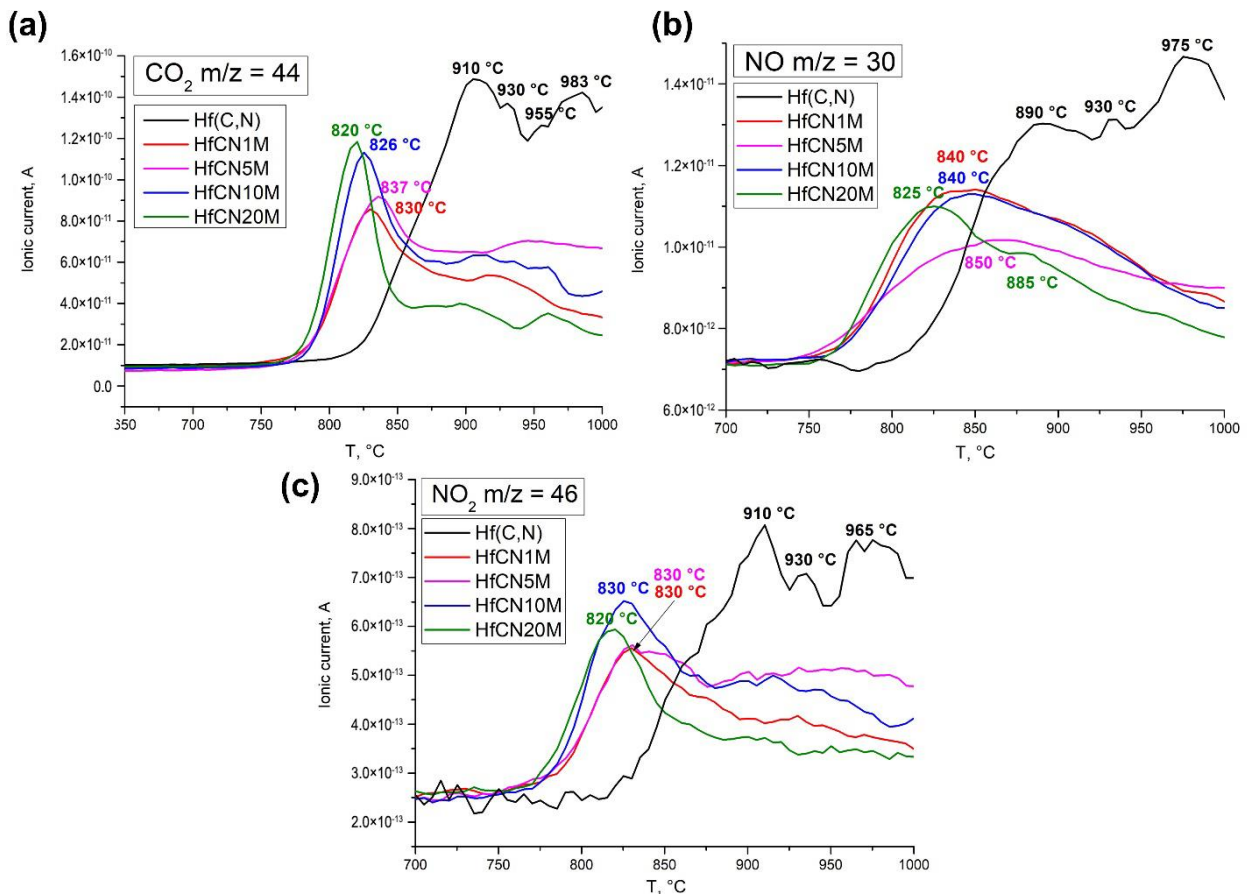


Figure 5. MS analysis during the oxidation of bulk Hf(C,N) and Hf(C,N)-MoSi₂ upon heating to 1000 °C. (a) CO₂, (b) NO, (c) NO₂.

Apparently, the initial formation of NO and NO₂ is due to the displacement of nitrogen atoms by oxygen atoms, as a result of which an extremely unstable Hf-C-O compound is formed [25]. The Hf-C-O rapidly transforms into the monoclinic HfO₂ phase with the evaporation of CO₂, which we observe with a slight delay (Figure 5). The process of gaseous

reaction product evolution continues at higher temperatures, and as a result, the sample is completely oxidized. The oxidation of HfCN1M and HfCN5M also proceeds without an intense heat release, and the formation of wide exothermic peaks is due to the release of CO₂, NO, and NO₂ (Figure 5).

During the oxidation of the HfCN10M and HfCN20M, an increase in the thermal effect of the reaction is observed, followed by the formation of a pronounced exothermic peak. An increase in the MoSi₂ content from 10 to 20 vol% leads to a shift in the exothermic peak maximum temperature to lower values. It is noted that the point on the TG curves corresponding to the maximum oxidation rate coincides with the temperatures of the exothermic peak—800 and 820 °C for HfCN10M and HfCN20M, respectively. The presence of this peak in samples with a high MoSi₂ content is probably due to a significant increase in the MoO₃ vapor pressure at a temperature of 800 °C. The subsequent peaks at higher temperatures, which were also observed on the other samples, are the result of the release of gaseous products during Hf(C,N) oxidation.

For all samples, the intensity of the CO₂ peaks is higher in comparison with NO and even more with NO₂, which is due to the composition of the initial Hf(C,N), which contains 3.1 wt% C and 2.5 wt% N [26]. Since NO₂ has the lowest intensity, we neglected it in further discussions.

It is worth noting that the introduction of MoSi₂ contributed to a decrease in the intensity of the CO₂ and NO peaks compared to pure Hf(C,N). However, when looking only at composites, an increase in the MoSi₂ content leads to an exponential increase in the intensity of the main CO₂ peak (Figure 6).

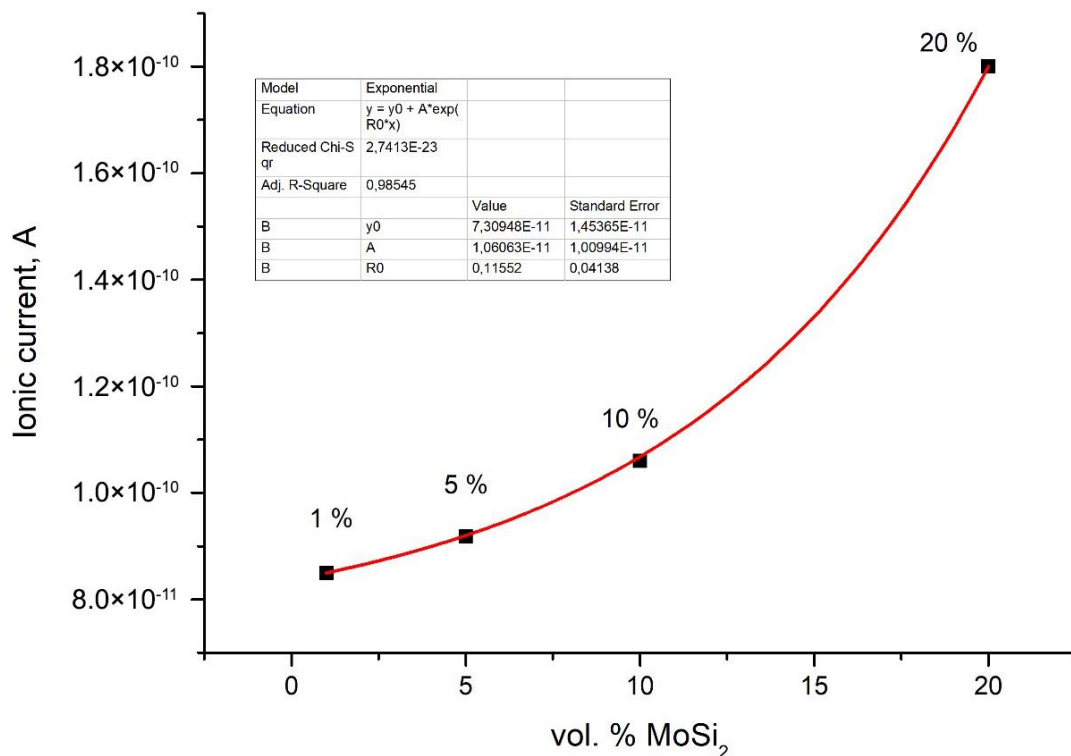


Figure 6. Dependence of the CO₂ main peak intensity on the MoSi₂ concentration.

Figure 7 shows the microstructures of the Hf(C,N) and Hf(C,N)-MoSi₂ samples after isothermal oxidation in a furnace at a temperature of 1000 °C for 30 min. Depending on the MoSi₂ content, different oxide layers with different structures and phase compositions are formed on the surface of the samples. The oxidation of Hf(C,N) is accompanied by the formation of a two-layer oxide film, consisting of a dense layer about 50 μm thick and a loose cracking layer (Figure 7a). The thickness of the dense layer is 1.05 mm. According to XRD results, the formed oxide film consists exclusively of monoclinic HfO₂ (Figure 8).

The addition of 1 and 5 vol% MoSi₂ contributes to a significant decrease in the rate of Hf(C,N) oxidation, which is apparently due to the formation of dense oxide layers on the surface (Figure 7b,c). These layers are 60 and 105 μm thick, respectively, and consist mainly of monoclinic hafnium oxide, as well as a small amount of hafnium orthosilicate HfSiO₄ (Figure 8). An increase in the MoSi₂ concentration in the samples affects not only the oxidation rate but also the structure of the oxide film. After isothermal oxidation of HfCN10M at 900 °C, a 190-μm-thick loose oxide layer with pores and microcracks is observed by SEM (Figure 7d). XRD analysis of the oxide films HfCN1M, HfCN5M, and HfCN10M are identical. When the concentration of MoSi₂ is increased from 10 to 20 vol%, a 305 μm-thick oxide film with a “flake-like” morphology is formed. (Figure 7e). Only monoclinic HfO₂ is found in this layer (Figure 8). It should also be noted that in the structure of the oxide layers of all Hf(C,N)-MoSi₂ samples, in addition to HfO₂ (light areas), local gray MoSi₂ and black SiO₂ inclusions are found (Figure 9).

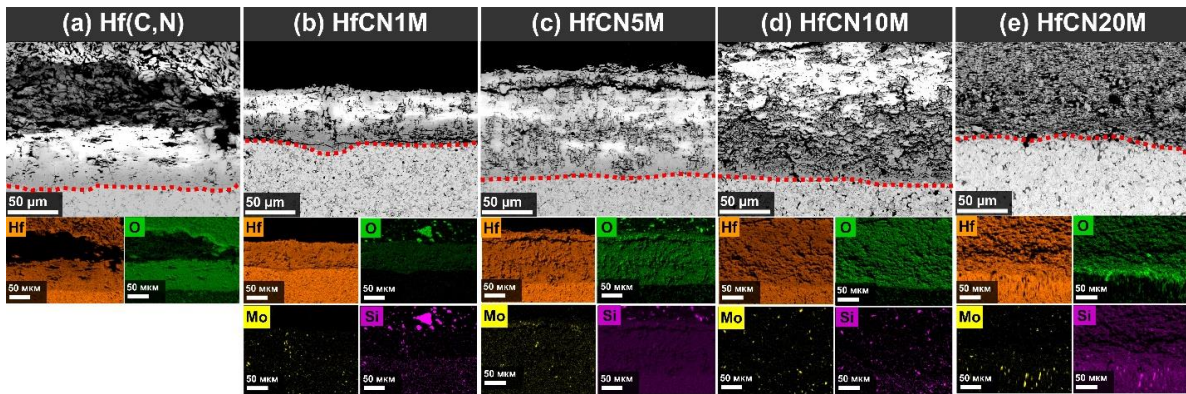


Figure 7. Micrographs of Hf(C,N) and Hf(C,N)-MoSi₂ samples after oxidation in a furnace at 1000 °C (red dashed line is the sample’s surface).

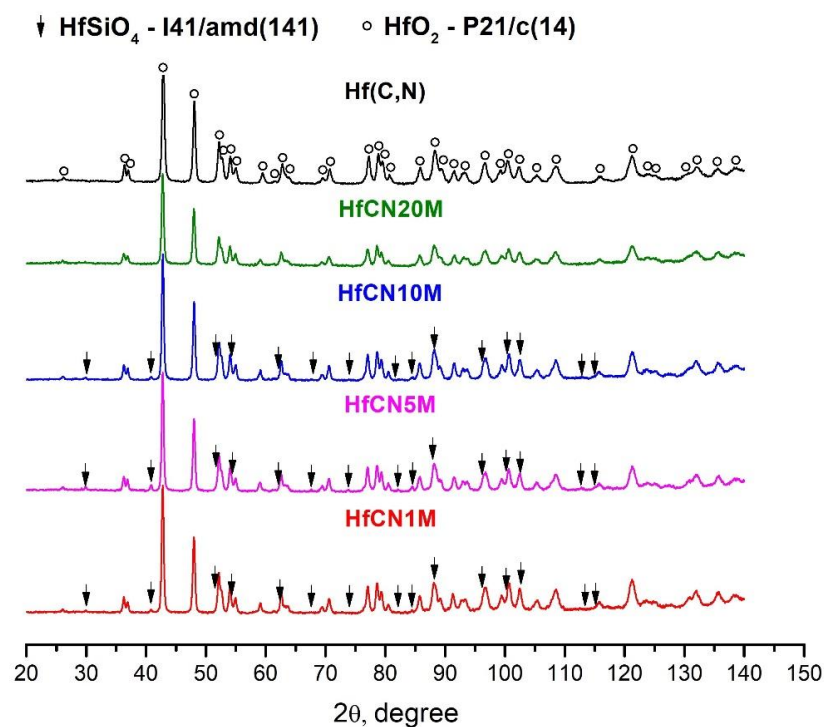


Figure 8. XRD data of the samples after oxidation in a furnace at 1000 °C.

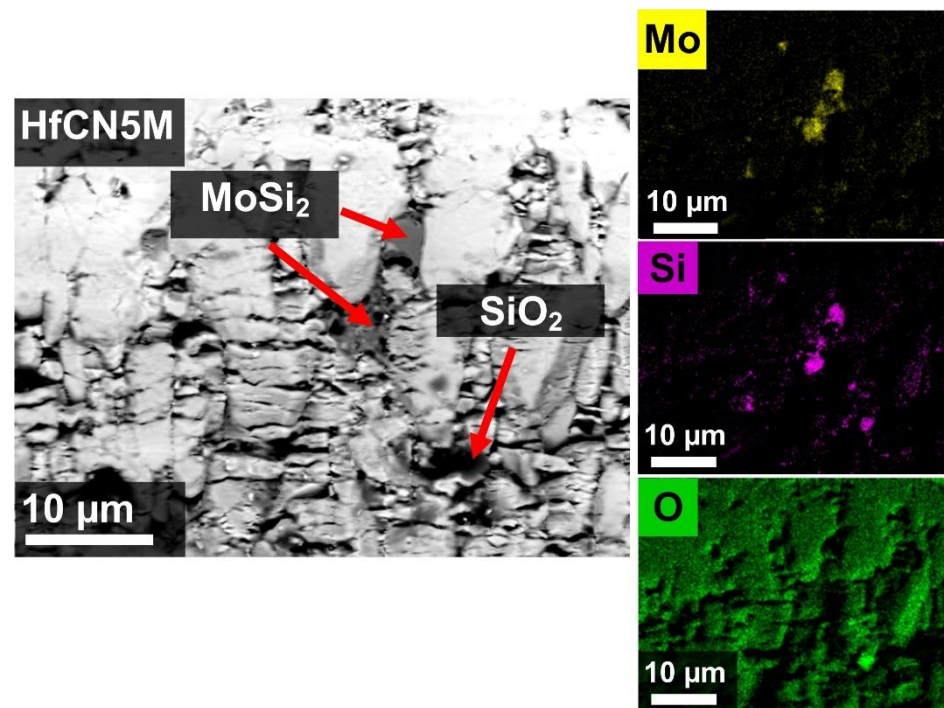


Figure 9. Local inclusions of MoSi_2 and SiO_2 in the HfCN5M oxide layer after isothermal oxidation in a furnace at 1000°C .

Figure 10 clarifies the dependence of the oxide layer thickness on the MoSi_2 concentration. The introduction of MoSi_2 contributes to a reduction in the thickness of the oxide film of at least 3.5 times, and its thickness increases linearly with increasing MoSi_2 content.

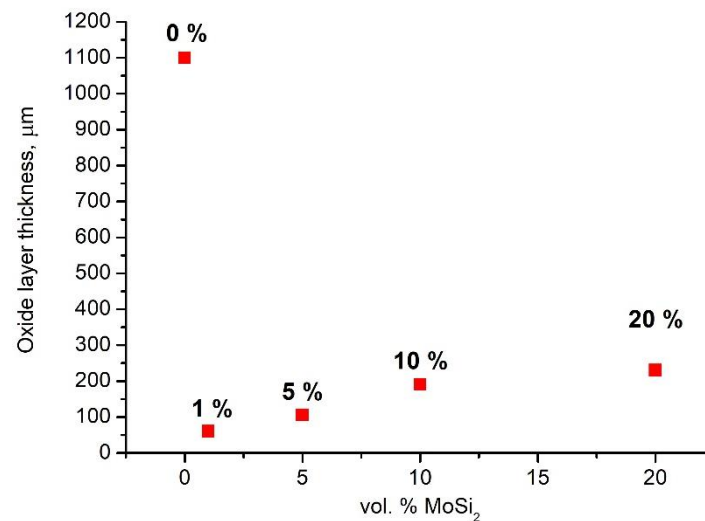
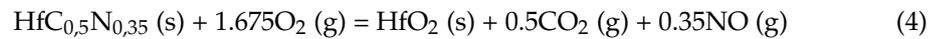


Figure 10. Thickness of the oxide film on the Hf(C,N) surface as a function of MoSi_2 content.

4. Discussion

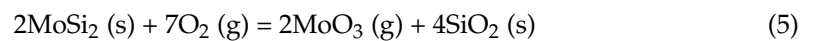
The high weight gain (10%) and oxide layer thickness (1.1 mm) of the Hf(C,N) sample are due to several factors. First, during oxidation, the formation of monoclinic HfO_2 on the Hf(C,N) surface was observed. It has a high oxygen diffusion rate ($k_p = 10^{-7} \text{ g}^2 \cdot \text{cm}^4 \cdot \text{s}^{-1}$) [13], and at temperatures above 900°C (the point of inflection on the TG curve for Hf(C,N)), it loses its protective properties and becomes loose and powdery, contributing to the active infiltration of oxygen into the material. Second, the process of Hf(C,N) oxidation was

accompanied by the release of C and N along the grain boundaries, which then react with oxygen to form predominantly CO₂ and NO:



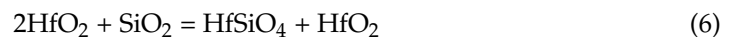
The release of gaseous products occurs through the monoclinic HfO₂ layer, which subsequently causes the formation of pores and cracks. This, in turn, facilitates the access of oxygen to the substrate, thereby accelerating the oxidation process. The introduction of MoSi₂ significantly increases the oxidative resistance of Hf(C,N), as was demonstrated by both the TG curves and the SEM results. This agrees with the results of other studies [15,17,20]. MoSi₂ concentrations of 1 and 5 vol% contribute to the formation of dense oxide layers on the Hf(C,N) surface, which prevent oxygen diffusion to the substrate. A higher content of molybdenum disilicide led to a thickening of the oxide films and the formation of a flake-like structure.

It is known that the oxidation of MoSi₂ proceeds in several stages [27]. Up to 800 °C, molybdenum disilicide oxidizes according to the reaction:



In this temperature range, the formation of MoO₃ with high volatility and vapor pressure predominates, while the rate of formation of protective SiO₂ is low. This results in strong internal stresses, which then lead to intense oxidation. Furthermore, according to the results of other studies, at temperatures between 750 and 800 °C, there is a rather sharp rise in the pressure of MoO₃ vapor, which is associated with the achievement of the boiling point of MoO₃ [28]. This fact explains the presence of an intense exothermic peak with a maximum at 800 °C in the HfCN20M with 20% MoSi₂ sample. According to the DSC curves and mass spectra of HfCN1M, HfCN5M, HfCN10M, and HfCN20M in the range from 800 to 1000 °C, we observed the predominance of Hf(C,N) oxidation according to reaction 4 with the formation of monoclinic HfO₂ and the release of mainly CO₂ and NO (Figure 5).

Reaction (5) with the formation of volatile MoO₃ decelerates; therefore, the TG curves show inhibition of the oxidation process. In samples containing 1, 5, and 10 vol% MoSi₂, after a 30-min exposure at 1000 °C, according to the reaction (6), we observed the formation of the HfSiO₄ phase, in which the oxygen diffusion rate is several orders of magnitude lower compared to HfO₂ [27,29]:



This phase was not detected in the sample with 20 vol% MoSi₂. The increase in the amount of CO₂ and the thickness of the oxide layer with an increase in the concentration of MoSi₂ can be due to an increase in the amount of gaseous MoO₃. Its transport through the oxide layer promotes the crystallization of amorphous SiO₂, the formation of pores, and cracks, thereby facilitating the access of oxygen to Hf(C,N)-MoSi₂. It is also possible that the release of a high concentration of MoO₃ along with CO₂ and NO prevents the diffusion interaction of HfO₂ and SiO₂ in the HfCN20M sample and, consequently, the formation of HfSiO₄.

5. Conclusions

In the present work, Hf(C,N)-MoSi₂ composites with varying MoSi₂ contents were produced by the SPS method. The materials exhibited a relative density of 98% and a hardness ranging from 16.9 to 19.2 GPa. The onset oxidation temperatures for the Hf(C,N) and Hf(C,N)-MoSi₂ were determined during non-isothermal oxidation at the DSC-TG up to 1000 °C at a heating rate of 20 °C/min in air. The effect of MoSi₂ content on weight gain and gas evolution during oxidation was also examined. The oxidation process began at 725 °C for both samples with MoSi₂ and pure Hf(C,N). For composites with low MoSi₂

content (1 and 5 vol%), hafnium carbonitride oxidation mainly occurred, during which monoclinic hafnium oxide was formed. Along with it, gaseous reaction products, mainly CO₂ and NO, with a small amount of NO₂, were released. When the concentration of MoSi₂ was increased to 10 and 20 vol%, a pronounced exothermic peak appeared on the DSC curve, which corresponded to an increase in the vapor pressure of volatile MoO₃. The smallest weight gain of 3.7% and 4.2% was demonstrated by samples containing 1 and 5 vol% MoSi₂, respectively.

The effect of MoSi₂ on the structure and phase composition of the oxide layer was established by isothermal oxidation in an electric furnace at 1000 °C for 30 min. The introduction of MoSi₂ contributed to a reduction in the thickness of the oxide film by at least 3.5 times when compared to Hf(C,N). On the surface of samples containing 1 and 5 vol% MoSi₂, a dense oxide layer, composed of monoclinic HfO₂ and a small amount of HfSiO₄, was formed. An increase in the MoSi₂ concentration resulted in swelling of the oxide layer due to the volatilization of a high concentration of MoO₃ together with CO₂ and NO at around 750–800 °C, thereby accelerating the oxidation. The absence of hafnium orthosilicate in the sample with 20 vol% MoSi₂ is due to abundant gas evolution, which prevents the diffusion interaction of HfO₂ and SiO₂. The introduction of MoSi₂ contributed to an increase in the oxidation resistance of Hf(C,N) due to the formation of refractory HfSiO₄ with a low oxygen diffusion rate.

Author Contributions: Conceptualization, V.S. and A.N.; methodology, V.S., A.N., D.S., K.K., P.L. and D.M.; investigation, V.S., A.N., D.S., K.K., P.L. and D.M.; resources, D.M.; data curation, V.S.; writing—original draft preparation, V.S.; writing—review and editing, V.S., A.N. and K.K.; visualization, V.S.; supervision, A.N.; project administration, A.N. and D.M.; funding acquisition, D.M. All authors have read and agreed to the published version of the manuscript.

Funding: This research received no external funding.

Institutional Review Board Statement: Not applicable.

Informed Consent Statement: Not applicable.

Data Availability Statement: Not applicable.

Conflicts of Interest: The authors declare no conflict of interest.

References

1. Sengupta, P.; Manna, I. Advanced High-Temperature Structural Materials for Aerospace and Power Sectors: A Critical Review. *Trans. Indian Inst. Met.* **2019**, *72*, 2043–2059. [[CrossRef](#)]
2. Campbell, N.S.; Boyd, I.; Chen, S. Unified Material-Environment Interaction Model for Binary UHTC Composites. In Proceedings of the AIAA AVIATION 2021 FORUM, Reston, VA, USA, 2–6 August 2021; American Institute of Aeronautics and Astronautics: Reston, VA, USA, 2021. [[CrossRef](#)]
3. Aritonang, S.; Ezha Kurniasari, W.S.; Juhana, R.; Herawan, T. Analyzing Tantalum Carbide (TaC) and Hafnium Carbide (HfC) for Spacecraft Material. In *Recent Trends in Manufacturing and Materials Towards Industry 4.0*; Springer: Singapore, 2021; pp. 925–933. [[CrossRef](#)]
4. Peng, Z.; Sun, W.; Xiong, X.; Xu, Y.; Zhou, Z.; Zhan, Z.; Zhang, H.; Zeng, Y. Novel Nitrogen-Doped Hafnium Carbides for Advanced Ablation Resistance up to 3273 K. *Corros. Sci.* **2021**, *189*, 109623. [[CrossRef](#)]
5. Yan, Y.; Wei, Q.; Yan, H.; Wu, Z.; Zhang, M. Stability and Electronic Properties of Five New Ternary Tantalum Carbonitrides. *Comput. Mater. Sci.* **2022**, *214*, 111728. [[CrossRef](#)]
6. Peng, Z.; Sun, W.; Xiong, X.; Zhang, H.; Guo, F.; Li, J. Novel Refractory High-Entropy Ceramics: Transition Metal Carbonitrides with Superior Ablation Resistance. *Corros. Sci.* **2021**, *184*, 109359. [[CrossRef](#)]
7. Wang, Y.; Csanádi, T.; Zhang, H.; Dusza, J.; Reece, M.J. Synthesis, Microstructure, and Mechanical Properties of Novel High Entropy Carbonitrides. *Acta Mater.* **2022**, *231*, 117887. [[CrossRef](#)]
8. Córdoba, J.M.; Sayagués, M.J.; Alcalá, M.D.; Gotor, F.J. Monophasic Nanostructured Powders of Niobium, Tantalum, and Hafnium Carbonitrides Synthesized by a Mechanically Induced Self-Propagating Reaction. *J. Am. Ceram. Soc.* **2007**, *90*, 381–387. [[CrossRef](#)]
9. Krasnenko, V.; Briik, M.G. First-Principles Calculations of the Structural, Elastic and Electronic Properties of MN_xC_{1-x} (M = Ti, Zr, Hf; 0 ≤ x ≤ 1) Carbonitrides at Ambient and Elevated Hydrostatic Pressure. *Solid State Sci.* **2014**, *28*, 1–8. [[CrossRef](#)]
10. Hong, Q.-J.; van de Walle, A. Prediction of the Material with Highest Known Melting Point from Ab Initio Molecular Dynamics Calculations. *Phys. Rev. B* **2015**, *92*, 020104. [[CrossRef](#)]

11. Zaoui, A.; Bouhaf, B.; Ruterana, P. First-Principles Calculations on the Electronic Structure of $TiC_xNb_{1-x}C$ and $HfC_xNb_{1-x}C$ Alloys. *Mater. Chem. Phys.* **2005**, *91*, 108–115. [[CrossRef](#)]
12. Buinevich, V.S.; Nepapushev, A.A.; Moskovskikh, D.O.; Trusov, G.V.; Kuskov, K.V.; Vadchenko, S.G.; Rogachev, A.S.; Mukasyan, A.S. Fabrication of Ultra-High-Temperature Nonstoichiometric Hafnium Carbonitride via Combustion Synthesis and Spark Plasma Sintering. *Ceram. Int.* **2020**, *46*, 16068–16073. [[CrossRef](#)]
13. Ni, N.; Hao, W.; Liu, T.; Zhou, L.; Guo, F.; Zhao, X.; Xiao, P. Oxidation/Ablation Behaviors of Hafnium Carbide-Silicon Carbonitride Systems at 1500 and 2500 C. *Ceram. Int.* **2020**, *46*, 23840–23853. [[CrossRef](#)]
14. Suvorova (Buinevich), V.S.; Nepapushev, A.A.; Moskovskikh, D.O.; Trusov, G.V.; Kuskov, K.V.; Kolesnikov, E.A. Fabrication and Oxidation Resistance of the Hafnium Carbonitride—Silicon Carbide Composites. *Ceram. Int.* **2022**, *48*, 23870–23877. [[CrossRef](#)]
15. Chen, R.; Zhang, Y.; Zhang, J.; Zhu, X. MoSi₂ Modified HfC Coating for the Ablation Protection of SiC-Coated C/C Composites: Ablation Resistance and Behavior. *Corros. Sci.* **2022**, *205*, 110418. [[CrossRef](#)]
16. Vorotilo, S.; Potanin, A.; Pogozhev, Y.; Levashov, E.; Kochetov, N.; Kovalev, D. Self-Propagating High-Temperature Synthesis of Advanced Ceramics MoSi₂–HfB₂–MoB. *Ceram. Int.* **2019**, *45*, 96–107. [[CrossRef](#)]
17. Potanin, A.Y.; Vorotilo, S.; Pogozhev, Y.S.; Rupasov, S.I.; Loginov, P.A.; Shvyndina, N.; Sviridova, T.A.; Levashov, E.A. High-Temperature Oxidation and Plasma Torch Testing of MoSi₂–HfB₂–MoB Ceramics with Single-Level and Two-Level Structure. *Corros. Sci.* **2019**, *158*, 108074. [[CrossRef](#)]
18. Kulczyk-Malecka, J.; Zhang, X.; Carr, J.; Carabat, A.L.; Sloof, W.G.; van der Zwaag, S.; Cernuschi, F.; Nozahic, F.; Monceau, D.; Estournès, C.; et al. Influence of Embedded MoSi₂ Particles on the High Temperature Thermal Conductivity of SPS Produced Yttria-Stabilised Zirconia Model Thermal Barrier Coatings. *Surf. Coat. Technol.* **2016**, *308*, 31–39. [[CrossRef](#)]
19. Ghadami, S.; Taheri-Nassaj, E.; Baharvandi, H.R.; Ghadami, F. Effect of in Situ SiC and MoSi₂ Phases on the Oxidation Behavior of HfB₂-Based Composites. *Ceram. Int.* **2020**, *46*, 20299–20305. [[CrossRef](#)]
20. Yang, Q.; Ren, X.; Zhang, M.; Zhu, L.; Chu, H.; Feng, P. Oxidation Inhibition Behaviors of HfB₂-MoSi₂-SiC Oxygen Blocking Coating Prepared by Spark Plasma Sintering. *J. Am. Ceram. Soc.* **2022**, *105*, 1568–1580. [[CrossRef](#)]
21. Yan, J.; He, Z.; Wang, Y.; Qiu, J.; Wang, Y. Microstructure and Wear Resistance of Plasma-Sprayed Molybdenum Coating Reinforced by MoSi₂ Particles. *J. Therm. Spray Technol.* **2016**, *25*, 1322–1329. [[CrossRef](#)]
22. Silvestroni, L.; Belloso, A.; Melandri, C.; Sciti, D.; Liu, J.X.; Zhang, G.J. Microstructure and Properties of HfC and TaC-Based Ceramics Obtained by Ultrafine Powder. *J. Eur. Ceram. Soc.* **2011**, *31*, 619–627. [[CrossRef](#)]
23. Sciti, D.; Silvestroni, L.; Guicciardi, S.; Fabbri, D.D.; Belloso, A. Processing, Mechanical Properties and Oxidation Behavior of TaC and HfC Composites Containing 15 Vol% TaSi₂ or MoSi₂. *J. Mater. Res.* **2009**, *24*, 2056–2065. [[CrossRef](#)]
24. Sciti, D.; Silvestroni, L.; Belloso, A. High-Density Pressureless-Sintered HfC-Based Composites. *J. Am. Ceram. Soc.* **2006**, *89*, 2668–2670. [[CrossRef](#)]
25. Fahrenholtz, W.G.; Hilmas, G.E. Ultra-High Temperature Ceramics: Materials for Extreme Environments. *Scr. Mater.* **2017**, *129*, 94–99. [[CrossRef](#)]
26. Feng, L.; Lee, S.-H.; Yin, J. Low-Temperature Sintering of HfC/SiC Nanocomposites Using HfSi₂-C Additives. *J. Am. Ceram. Soc.* **2016**, *99*, 2632–2638. [[CrossRef](#)]
27. Shin, D.; Arróyave, R.; Liu, Z.-K. Thermodynamic Modeling of the Hf–Si–O System. *Calphad* **2006**, *30*, 375–386. [[CrossRef](#)]
28. Wirkus, C.D.; Wilder, D.R. High-Temperature Oxidation of Molybdenum Disilicide. *J. Am. Ceram. Soc.* **1966**, *49*, 173–177. [[CrossRef](#)]
29. Zhang, Z.; Park, Y.; Xue, Z.; Zhang, S.; Byon, E.; Koo, B.H. Effect of the HfO₂/SiO₂ Pre-Mixing Ratio and Heating Temperature on the Formation of HfSiO₄ as a Bond Coat of Environmental Barrier Coatings. *Ceram. Int.* **2022**, *48*, 15657–15667. [[CrossRef](#)]

Disclaimer/Publisher’s Note: The statements, opinions and data contained in all publications are solely those of the individual author(s) and contributor(s) and not of MDPI and/or the editor(s). MDPI and/or the editor(s) disclaim responsibility for any injury to people or property resulting from any ideas, methods, instructions or products referred to in the content.